

NASA/TM-20220009943



Design, Control, and Simulation of Tensegrity Based Kites

Nathan Scheinkman

California Polytechnic State University, San Luis Obispo

Bjorn Johnson

University of California, San Diego

Abed Musaffar

University of California, Santa Barbara

Dr. Adrian Agogino

NASA Ames Research Center

June 2022

NASA STI Program... in Profile

Since its founding, NASA has been dedicated to the advancement of aeronautics and space science. The NASA scientific and technical information (STI) program plays a key part in helping NASA maintain this important role.

The NASA STI Program operates under the auspices of the Agency Chief Information Officer. It collects, organizes, provides for archiving, and disseminates NASA's STI. The NASA STI Program provides access to the NASA Aeronautics and Space Database and its public interface, the NASA Technical Report Server, thus providing one of the largest collections of aeronautical and space science STI in the world. Results are published in both non-NASA channels and by NASA in the NASA STI Report Series, which includes the following report types:

- **TECHNICAL PUBLICATION.** Reports of completed research or a major significant phase of research that present the results of NASA programs and include extensive data or theoretical analysis. Includes compilations of significant scientific and technical data and information deemed to be of continuing reference value. NASA counterpart of peer-reviewed formal professional papers, but having less stringent limitations on manuscript length and extent of graphic presentations.
- **TECHNICAL MEMORANDUM.** Scientific and technical findings that are preliminary or of specialized interest, e.g., quick release reports, working papers, and bibliographies that contain minimal annotation. Does not contain extensive analysis.
- **CONTRACTOR REPORT.** Scientific and technical findings by NASA-sponsored contractors and grantees.

- **CONFERENCE PUBLICATION.** Collected papers from scientific and technical conferences, symposia, seminars, or other meetings sponsored or co-sponsored by NASA.
- **SPECIAL PUBLICATION.** Scientific, technical, or historical information from NASA programs, projects, and missions, often concerned with subjects having substantial public interest.
- **TECHNICAL TRANSLATION.** English-language translations of foreign scientific and technical material pertinent to NASA's mission.

Specialized services also include organizing and publishing research results, distributing specialized research announcements and feeds, providing information desk and personal search support, and enabling data exchange services.

For more information about the NASA STI Program, see the following:

- Access the NASA STI program home page at <http://www.sti.nasa.gov>
- E-mail your question to help@sti.nasa.gov
- Phone the NASA STI Information Desk at 757-864-9658
- Write to:
NASA STI Information Desk
Mail Stop 148
NASA Langley Research Center
Hampton, VA 23681-2199

NASA/TM-20220009943



Design, Control, and Simulation of Tensegrity Based Kites

Nathan Scheinkman

California Polytechnic State University, San Luis Obispo

Bjorn Johnson

University of California, San Diego

Abed Musaffar

University of California, Santa Barbara

Dr. Adrian Agogino

NASA Ames Research Center

National Aeronautics and
Space Administration

Ames Research Center
Moffett Field, California 94035

June 2022

The use of trademarks or names of manufacturers in this report is for accurate reporting and does not constitute an official endorsement, either expressed or implied, of such products or manufacturers by the National Aeronautics and Space Administration.

Available from:

NASA STI Program / Mail Stop 148
NASA Langley Research Center
Hampton, VA 23681-2199
Fax: 757-864-6500

Abstract

Due to lowering price and increased functionality, the future could bring in a huge number of UAVs flying in urban areas. In order to safely accommodate them, they should be fundamentally safe to fly. Unfortunately, current rigid designs could cause significant damage in case of a crash. To mitigate this problem, this report proposes constructing soft UAVs using tensegrity structures in order to mitigate the impact of collisions, effectively improving the safety of the vehicles and increasing public confidence in the use of UAVs. In this paradigm, the frame of the vehicle is designed using a tensegrity structure, a geometric structure composed of suspended elements of pure compression and pure tension, which during a collision can better absorb high stresses through elastic deformation. As a feasibility study we test this concept on an actuated tensegrity kite in a custom physics simulator, designed to simulate tensegrity structures with non-rigid rods, along with basic simulations of lift. Results show that this concept is feasible and that the kite can change orientation by actively changing the shape of the tensegrity structure.

1 Introduction

Current UAVs typically consist of rigid frames. This rigidity leads to well-understood control policies and quick responses to inputs, but becomes a serious detriment in the event of a collision. When a rigid UAV crashes it risks not only snapping its frame and damaging critical electrical components inside, but also can damage the object with which it collides. As an alternative to rigid designs, we propose designing UAVs out of non-rigid tensegrity structures. These structures are lightweight and compressible, which makes them prime candidates for use in novel aerial systems when collision safety is a concern.

Tensegrity structures are three dimensional geometric constructions of rods balanced and held in place by a network of tensioned cables. Recently, these structures have gained popularity for their promising advances in the field of robotics ranging from terrestrial locomotion to wearable exosuits. Aerial vehicles based on tensegrity structures would be able to deform in flight as a steering mechanism, as well as compress upon impact to reduce collision damage, giving them a significant safety advantage over the classic rigid designs.

Unfortunately, the properties which make tensegrities advantageous for flight also make them difficult to analyze using conventional methods. The goal of this report is to detail the procedure for designing and controlling a preliminary model for a tensegrity aerial vehicle (a tensegrity kite) in simulation. While the behavior of these structures is not well understood, each component of the structure has known behavior, and therefore can be modeled in simulation. We model each basic component and assemble them into the final structure to analyze as a whole, giving an approximation of the entire system's behavior. Currently available simulation software is not equipped to accurately model the complex dynamics of a tensegrity structure and therefore efforts were made to expand the capability of our previous rigid body physics simulation tool to include tensegrity components and

simple airfoil aerodynamics such that it is capable of approximating the behavior of soft-robotic aerial vehicles in real time. A by-product of this work is therefore a platform for assisting in the design of tensegrity based unmanned aerial systems (UAS) through visualizations of vehicle behavior, allowing for analysis of system responses to changes in physical configuration and wind conditions.

2 Background

Tensegrity structures have been used in the past largely in artistic works and toys, as they can be built in a variety of interesting shapes and often move in excitingly unpredictable ways. Recent research has shown that these structures hold much more promise than initially thought, and can be used effectively in a wide variety of applications [1–5]. Most interestingly for this work, it has been shown that both multi-rotor and kite-like vehicles based on tensegrity would exhibit some desirable properties, and are theoretically feasible to build and fly [6]. We focus on the kite-like vehicles in this work.

In order to simulate such a vehicle’s behavior, we need a tool capable of combining aerodynamic forces with rigid body dynamics to show evolution of the system in real time. Current state of the art simulation methods include a host of tools for computational fluid dynamics (CFD), capable of giving accurate insights about flow around a surface or vehicle and the numerous forces involved. These methods work incredibly well for tasks such as optimizing a wing shape, but do not lend themselves well to the evolving real time dynamics we expect to see in a tensegrity system. In addition, our work requires a significantly lower degree of accuracy than CFD provides, as we seek to only approximate the behavior of the entire system and don’t necessarily need every force involved to be accurate. Furthermore, any aerodynamic approach would need to be combined with a rigid body physics simulation environment, which can be used to approximate the dynamics of a number of interacting bodies. When the number of bodies involved is small these tools can run at many times faster than the real world, but can have inaccuracies in the forces involved and do not provide any aerodynamic analysis whatsoever. In addition, these systems are often limited to rigid bodies, and thus are difficult to use for simulating tensegrity structures with flexible elements.

In order to address the issues listed above, we build the AirTens platform by extending a lightweight rigid body simulation tool to include simple aerodynamic elements as well as flexible rods. The result is a platform capable of simulating in close to real time a kite-like tensegrity vehicle composed of bending rods and airfoils in a realistic way, allowing for analysis of various interesting behavioral characteristics which otherwise would not be possible without physically building the vehicle.

3 Methods

3.1 Vehicle Design

Our experimental vehicle was a tethered tensegrity kite composed of two bending rods, one lengthwise and one crosswise, suspended in a roughly diamond shape by four cables connecting their ends. Two additional cables on the bottom suspended the rods in such a way that they were roughly perpendicular to each other. The kite has two main foils, one large wing in front and one smaller wing in the rear for stabilization.

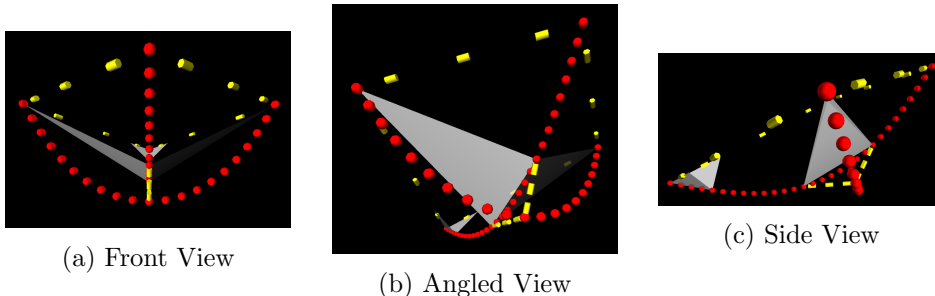


Figure 1: Design of the Tensegrity Kite. Kite is composed of bendable rods (red), connected with inelastic cables (yellow). Airfoils (gray) are stretched between ends of rods.

3.2 Experiments

We evaluate our simulation by simulating a tensegrity based kite, modifying the configuration and subjecting it to different wind conditions to assess realism of the entire system’s behavior. We run a number of experiments by initializing the kite at different positions and orientations in space while subject to different wind conditions to see if the vehicle can achieve an equilibrium state in a seemingly realistic manner. Analysis is performed visually where we are mainly looking for physically impossible or unlikely motions and any severe deformations in the vehicle. The vehicle is also actuated in a number of conditions to steer left and right and to achieve new equilibrium positions, also to be visualized in real time for unexpected behaviors. The two main experiments discussed in the paper are a stability experiment and a subsequent steering experiment.

3.2.1 Kite Size and Stability

The stability of the kite tends to increase with its size. To determine the smallest kite with reasonable stability characteristics, we perform a set of experiments. In these experiments we scale the initial kite design to different sizes while maintaining the same geometry. For each scaling factor, we divide all linear stiffness and damping constants by the scaling factor, while multiplying all rest lengths and torsional stiffness constants by the same scaling factor. Mass is kept constant at 1.2 kilograms.

This results in a kite that maintains the original geometry, but at a different size. In these experiments the wind velocity is stochastic on a uniform distribution from 5 to 7 m/s.

3.2.2 Steering

In the next experiment we simulate actuating the cables of the kite. In this simulation the motor actuates the cables connecting the center rod to the lateral rod, pulling one wing tip towards the rear while the opposite reaches towards the front of the vehicle. This causes the kite to bank. The effectiveness of this turning method is determined qualitatively through visual inspection, and quantitatively by measuring the relative angle between the kite tether and the wind.

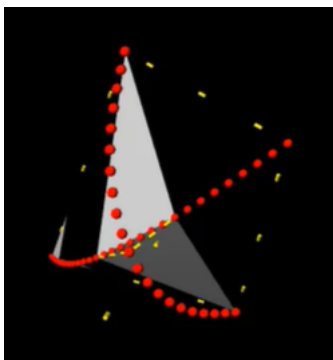


Figure 2: A Tensegrity Kite Banking Left

3.3 Simulation

We build our simulation platform by extending the open source `cannon-es` and `three.js` frameworks, which perform physics integration and rendering, respectively [7, 8]. Our work involves packaging the two frameworks into a cohesive platform which gave the user control over simulation speed and other high level characteristics. In addition, we create a number of custom objects which can be added to the simulated world with more interesting behaviors than previously allowed under the existing frameworks. The majority of this work was split between implementing reasonably accurate bending rod physics (see Appendix A) and simulating lift and drag on flat aerodynamic foils (see Appendix B), which together allowed for tensegrity based kites to be assembled and flown in the simulated world. This is accomplished by constructing novel physics objects based on rigid bodies and implementing custom update steps to achieve the desired object behavior, in our case realistic bending forces and simple aerodynamics.

4 Results

The simulation of the tensegrity kite has promising results, including visually realistic flight, elastic response to collisions, and successful flight control through cable

actuation.

4.1 Kite Stability

During flight, the simulated tensegrity kite often begins oscillating once reaching its equilibrium position. We can not determine the exact mechanism that causes the oscillations, although the period and magnitude of oscillation is heavily influenced by the size of the kite. These oscillations determine the stability of the kite, and as discussed in the previous section we desire to find the smallest kite size where the random noise of the wind, as opposed to the oscillation, is the main contributing factor to the flight path of the kite.

The oscillations of various kite sizes are seen in Figure 3. The oscillations are measured through the horizontal distance between the center of mass of the kite, and the line that passes through the anchor point of the kite in the direction of the mean wind. The horizontal lines in the 2.9 meter and 3.3 meter kites indicate collisions with the ground that flip the kites upside down, ceasing flight. The irregular shape of the 3.9 meter kite oscillation is due to two collisions with the ground where flight continued. The movement of the mean position of the 5.8 meter kite is due to the random noise introduced to the wind overcoming the small oscillations of the kite. From this data, we concluded that 5.8 meters is roughly the smallest kite that can maintain stability in simulation, and thus we choose it as the main design for actuation experiments.

4.2 Steering

The kite successfully steers itself by using a simulated motor to change the cable properties, resulting in a change in geometry that affected the flight path. The steering angle is measured by projecting the tether of the kite and the wind direction to the horizontal ground plane, then measuring the angle between the two projections using the dot product. This allows the measurement of the steering angle to be decoupled from the vertical angle caused by the lift. This steering angle is seen in Figure 4 for a wind speed of 6 meters per second, with and without noise.

From the figure it can be seen that the controlled turn results in a significant deviation in the equilibrium position of the kite, between 7.5 degrees and 33 degrees in an environment with wind noise, and approximately 17.5 degrees in an environment without wind noise. Visually, this results in the kite steering towards the desired direction and maintaining a new equilibrium position for the duration of the turn. This demonstrates successful control of a tensegrity aerial vehicle in simulation.

4.3 Kite Properties

Some properties of the final 5.8 meter kite design include a 1.2 kilogram mass, cable tensions under 300 Newtons, and cable stiffnesses under 500 Newtons per meter. These can be altered without significantly changing the flight characteristics of the kite, although less tension in the design makes it less stiff and less robust towards collisions. The tension of the various cables during the execution of a turn can be

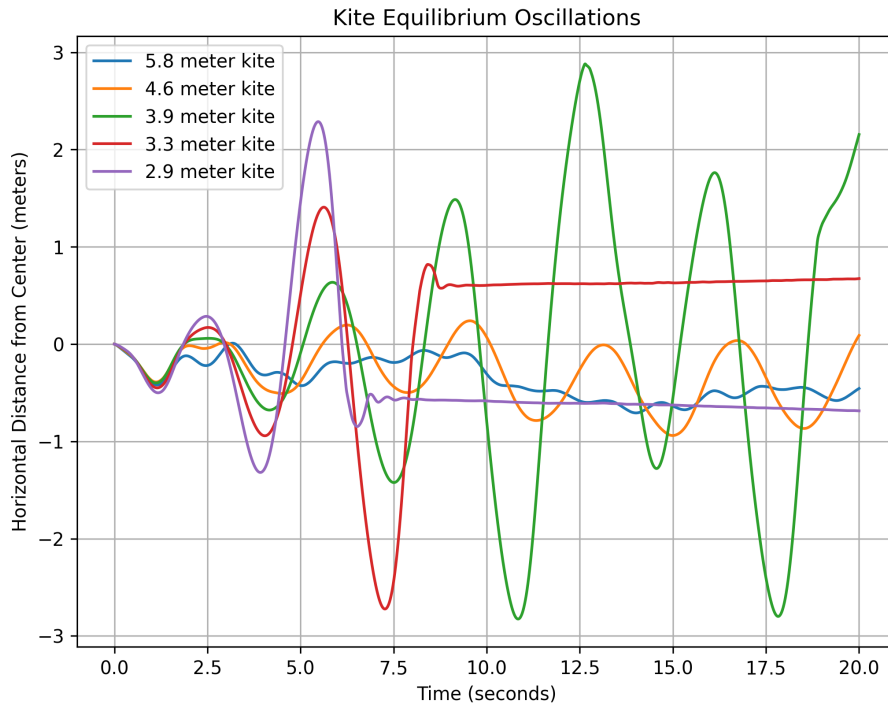


Figure 3: A graph of the oscillations of the kite depending on its size, subjected to a wind velocity of 6m/s with some random noise. Horizontal lines indicate collisions with the ground that ceased flight.

seen in Figure 5. The extreme behavior at the very beginning of the graph is caused by the convergence of the bending rods to their equilibrium positions.

5 Conclusion

Through our experiments and analysis, we show that our tensegrity based kite vehicle can be actuated relatively easily to steer by changing the shape of the vehicle. This makes the tensegrity based kite a promising steps towards an untethered UAV with tensegrity design principles.

Further research needs to be done on verifying the results of the simulation on a real life tensegrity kite prototype. This would evaluate the accuracy of our experiments and our simulation platform. We also believe that design principles from our kite like vehicle could be adapted into an untethered UAV system, which would allow for use in some of the settings currently dominated by small scale rigid UAVs.

In our efforts to approximate the behavior of experimental vehicle we also created a novel simulation platform which can be used for rapid design and experimentation on tensegrity based aerial vehicles, a capability which other platforms lack. We are

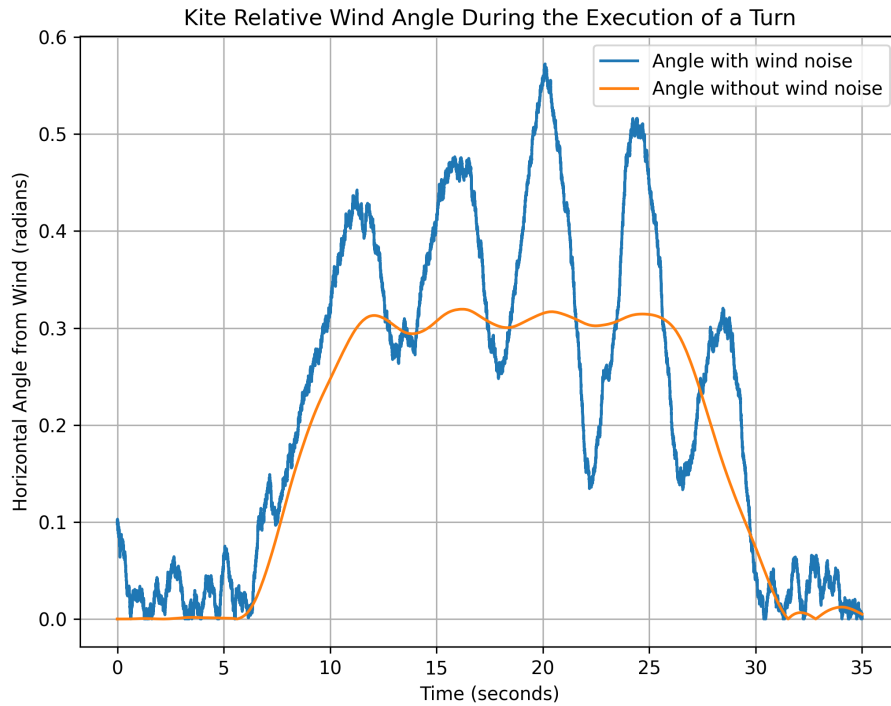


Figure 4: The deviation angle of the tensegrity kite during the execution of a turn, with and without random noise on the wind.

largely confident that this tool is realistic at least as a first degree approximation, and can give useful insights about vehicle behavior at a high level, even though the forces involved might not be exactly accurate. Our developed software platform can allow for researchers to quickly test related ideas in a simulated environment to cut prototyping costs and gain insights quickly.

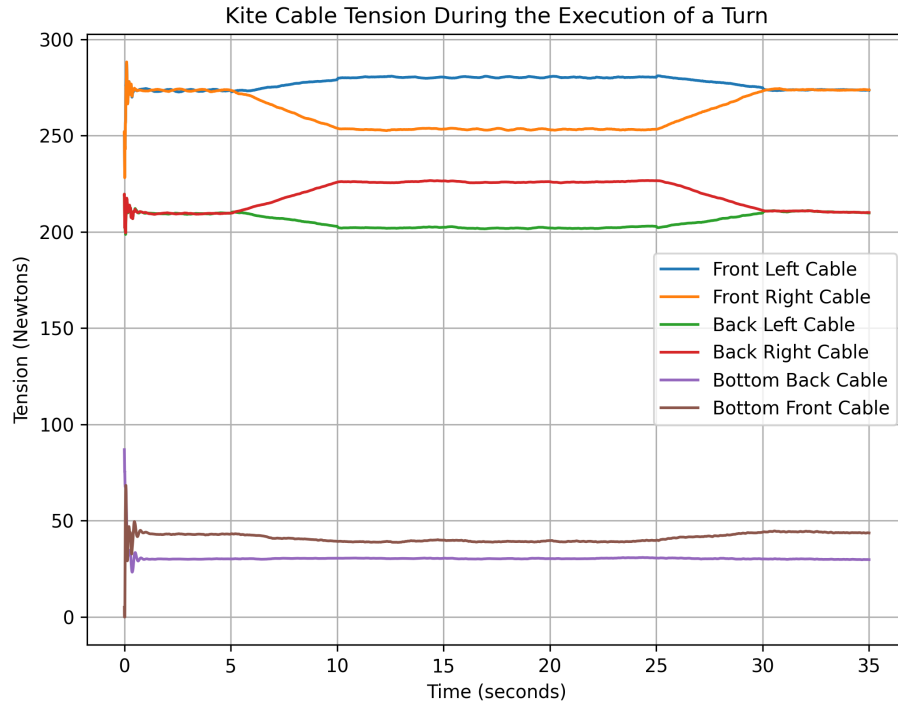


Figure 5: Kite cable tensions during a turn.

Appendix A

Bending Rod Approximation

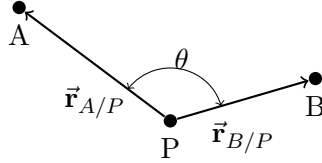
The tensegrity kite required the inclusion of structural rods subjected to large bending displacements. These rods would also be subjected to multiple outside forces along the length of the rod. This presented a computational challenge for a couple reasons. First, the physics simulation library that was used only simulates rigid bodies, so any implementation of bending would need to operate in a manner that is compatible with rigid bodies in the simulation. Second, it was desired for the simulation to run at close to real time. Typical analysis of bending components is usually done with linear approximations for small displacements, or complicated and intensive finite element analysis for large displacements and more accurate results. Since a tensegrity kite was composed of multiple bending rods connected together in a tension network, implementing an accurate finite element method would be excessively complicated and computationally intensive. However, the goal was not to create a highly accurate simulation of all the forces involved, but rather to simulate approximated behavior, so a faster, less accurate approach was used.

The approach taken was to discretize the bending rod into multiple spherical

rigid bodies, and then simulate linear springs between those bodies to create the correct behavior of tension and compression. Torsional springs were simulated between those same bodies to create the correct behavior of bending. Linear springs were included by the physics library and so they were easy to implement. Each neighboring pair of bodies in the rod had their own duplicate linear spring that worked together to create the behavior of tension and compression. Discretizing the linear springs allowed the same rod to experience tension at one part and compression at another. Torsional springs were not included in the library, and had to be implemented by hand. Each set of three neighboring bodies had their own duplicate torsional spring, and together, they created the behavior of bending. Discretizing the torsional springs allowed the same rod to have different curvature at different points. For a rod discretized into N points, $N - 1$ linear springs and $N - 2$ torsion springs were created.

A.0.1 Torsion Spring Implementation

The implementation of a torsional spring for three neighboring bodies, n_A , n_P , and n_B required knowledge of their positions, points A , P , and B , as well as a desired torsional stiffness k . From these, effective forces on each body, \vec{F}_A , \vec{F}_P , and \vec{F}_B can be found.



The relative positions between the bodies, along with their corresponding unit vectors are described by the following:

$$\vec{r}_{A/P} = A - P$$

$$\vec{r}_{B/P} = B - P$$

$$\hat{r}_{A/P} = \frac{\vec{r}_{A/P}}{|\vec{r}_{A/P}|}$$

$$\hat{r}_{B/P} = \frac{\vec{r}_{B/P}}{|\vec{r}_{B/P}|}$$

The angle θ between the vectors can be found by:

$$\theta = \cos^{-1} (\hat{r}_{A/P} \cdot \hat{r}_{B/P})$$

The rest angle for a rod is π , so the angle ϕ for the simulated torsion spring is as follows:

$$\phi = \theta - \pi$$

The moments generated by the spring could then be found:

$$\begin{aligned}\hat{\mathbf{M}}_A &= \frac{\hat{\mathbf{r}}_{B/P} \times \hat{\mathbf{r}}_{A/P}}{|\hat{\mathbf{r}}_{B/P} \times \hat{\mathbf{r}}_{A/P}|} \\ \vec{\mathbf{M}}_A &= -k\phi\hat{\mathbf{M}}_A \\ \vec{\mathbf{M}}_B &= -\vec{\mathbf{M}}_A\end{aligned}$$

Note that

$$\hat{\mathbf{M}}_A = \frac{\hat{\mathbf{r}}_{B/P} \times \hat{\mathbf{r}}_{A/P}}{|\hat{\mathbf{r}}_{B/P} \times \hat{\mathbf{r}}_{A/P}|}$$

is undefined when

$$\hat{\mathbf{r}}_{B/P} \times \hat{\mathbf{r}}_{A/P} = 0$$

This only occurs when the relative positions of the bodies are collinear, and thus the desired torque would be 0 when the relative positions are opposite each other, and unknown when in the same direction. This is mitigated in the implementation by generating no force in this scenario.

Moving on, the forces on the bodies $\vec{\mathbf{F}}_A$ and $\vec{\mathbf{F}}_B$ are generated by dividing the moment by the lever arm

$$\begin{aligned}\vec{\mathbf{F}}_A &= \frac{1}{|\vec{\mathbf{r}}_{A/P}|} \vec{\mathbf{M}}_A \times \hat{\mathbf{r}}_{A/P} \\ \vec{\mathbf{F}}_B &= \frac{1}{|\vec{\mathbf{r}}_{B/P}|} \vec{\mathbf{M}}_B \times \hat{\mathbf{r}}_{B/P}\end{aligned}$$

And lastly, following Newton's third law:

$$\vec{\mathbf{F}}_P = -(\vec{\mathbf{F}}_A + \vec{\mathbf{F}}_B)$$

For a rod made up of N point particles, bending can be emulated by implementing these torsion springs for sets of three neighboring point particles. Note that this requires that $N \geq 3$.

A.0.2 Limitations

There are many limitations to this method of simulating bending rods. The bending of real rods depends on the geometry and material of the rod, which this method ignores, although it could possibly be similar by choosing clever values for k . Precision errors for large values of N create divergent behavior for the torsion springs that in practice seem to require the time step of the physics simulation to be inversely proportional to N for large N .

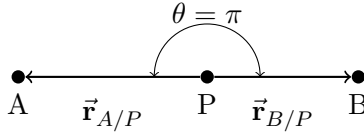
A damped torsion spring could not be found this way. In order to create damping, the rate of change of the angle between $\hat{\mathbf{r}}_{A/P}$ and $\hat{\mathbf{r}}_{B/P}$ must be known. This is difficult to simulate without numerical derivatives. To see why, note that:

$$\frac{d}{dt} (\hat{\mathbf{r}}_{A/P} \cdot \hat{\mathbf{r}}_{B/P}) = \frac{d}{dt} (\cos(\theta))$$

$$\hat{\mathbf{r}}_{A/P} \cdot \hat{\mathbf{r}}_{B/P} + \hat{\mathbf{r}}_{A/P} \cdot \dot{\hat{\mathbf{r}}}_{B/P} = -\sin(\theta) \frac{d\theta}{dt}$$

$$\frac{\dot{\hat{\mathbf{r}}}_{A/P} \cdot \hat{\mathbf{r}}_{B/P} + \hat{\mathbf{r}}_{A/P} \cdot \dot{\hat{\mathbf{r}}}_{B/P}}{-\sin(\theta)} = \frac{d\theta}{dt}$$

This creates undefined behavior when $\sin(\theta)$ is equal to 0, and bad behavior when $\sin(\theta)$ is close enough to 0 to create precision errors. This could not be ignored like it was for the moment vector, because the rate of change of the angle could be significant in this scenario. This scenario is also common, as it is the desired rest angle of the bar.



Another limitation encountered was that implementing bending rods through multiple torsion springs created wave-like effects through the bar as each time step of the physics simulation would propagate a displacement to neighboring torsion springs. Normal bending rods do propagate waves, so this can create correct behavior if the time step of the simulation was dependent on the speed of sound of the rod, but since this was not the case (as doing so carried a large computational cost) it created undesired behavior as the wave speed was heavily dependent on the time step. This effect was prevalent due to the lack of damping in the torsion springs.

The last limitation encountered was divergent behavior for large values of N and ϕ . Each point particle had a mass inversely proportional to N . If there was a large angular displacement ϕ for that particle, it would create a large force applied to a light object. This introduced precision errors, which typically created a larger than desired displacement. This large displacement would then propagate as a wave, creating even larger displacements that would compound and break the rod in spectacular fashion.

A.0.3 Mitigations

Since the focus was on similar behavior as opposed to accurate behavior, non standard solutions could be applied to the implementation of these bending rods.

To mitigate the error caused by the lack of angular damping, dampers were created that connected the ends of the rods. These dampers were linear springs that had zero stiffness, but high damping constants. As waves propagated through the rod, they would reach the ends of the rod where the energy would then be absorbed by these dampers. Increasing the damping to the linear springs between the point particles also helped mitigate this effect.

Implementing multiple linear and torsion springs to create a bending rod also created an issue of coupling. It was desired for the bending rod to have uniform behavior and mass distribution. This simplified a bending rod to six parameters (not

including angular dampers). Each linear spring was the same, with the characteristic equation

$$F = -c(x - l) - d\dot{x} \quad (\text{A1})$$

where F is the generated force

c is the spring constant

x is the relative distance between the two bodies

l is the rest length of the spring

d is the damping constant

\dot{x} is the projected relative velocity of the two bodies

And each torsion spring was the same, with the characteristic equation

$$T = -k\phi \quad (\text{A2})$$

where T is the generated torque

k is the torsion spring constant

ϕ is the relative angle between two bodies

Thus the physics of a bending rod created through this implementation required six input parameters, namely:

N = number of points in the rod

M = total mass of the rod

L = linear rest length of the rod

C = linear spring force constant of the rod

D = linear spring damping constant of the rod

K = torsion spring constant of the rod

To reduce coupling between the behavior of the rod and the number of points used to discretize the rod, it was necessary for the characteristics of the component bodies to depend on the number of bodies. This allowed the rod to converge towards a single behavior as the number of points got larger.

The mass m of a component body in a rod can be found as:

$$m = \frac{M}{N}$$

Since $N - 1$ component linear springs were created, and the expected behavior on the input parameter was for the behavior of the rod as a whole, the rest length l for each component linear spring is given by:

$$l = \frac{L}{N - 1}$$

and the linear spring stiffness c and linear spring damping d is given by:

$$c = C(N - 1)$$

$$d = D(N - 1)$$

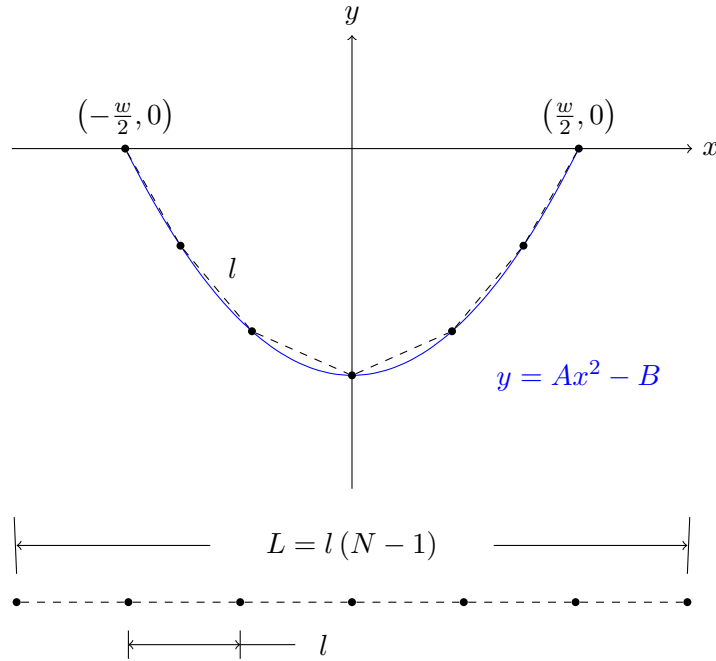
Similarly, because $N - 2$ component torsion springs were created, the torsion spring constant k for each component torsion spring is given by:

$$k = K(N - 2)$$

This allows for tuning of the value of N to create sufficient accuracy of the bending rod for the application, as increasing N would now cause the rod to converge to a single behavior (for a sufficiently small time step).

The easiest mitigation strategy for most divergent behavior found was decreasing the time step, but this carried with it a large computational cost. It was found that most of the accuracy was needed for the beginning of the simulation, as the component bodies of the rod when placed poorly would move erratically to their equilibrium position. Thus, finding a good initial position for the component bodies of the rod increased performance by allowing the time step to increase while maintaining convergent behavior.

All the bending rods in a tensegrity kite are part of a tension network that cause the rod to bend into an arched curve. Finding the correct curvature of that arch to place the component bodies is a difficult problem, and using that curvature to solve for the equidistant positions of each component body is an even harder problem, so the curve was approximated as a parabolic segment.



The rods in a tensegrity kite are usually bent in such a way that it creates similar behavior to a rod bent by a taut cable, such as in a bow. Thus the only known values are the length of the rod L , and the length of the taut cable w . To create the desired effect of symmetry, the chosen parabolic curve needed to be symmetric about the y -axis, and have a chord length of w between the points that crossed the x -axis. Thus, for $A \geq 0$, $B \geq 0$, the general parabolic equation is:

$$y = Ax^2 - B$$

A and B are unknown, and need to be determined by the properties of the cable and the rod.

If $S(x)$ denotes the arc length of the parabolic segment from $(-\frac{w}{2}, 0)$ to the point $(x, Ax^2 - B)$, then the total arc length of the parabolic segment can be approximated as

$$S\left(\frac{w}{2}\right) \approx L$$

Using the formula for the arc length of a curve,

$$S(x) = \int_{-\frac{w}{2}}^x \sqrt{1 + 4A^2t^2} dt$$

Integrating, it's found that

$$S(x) = \frac{Aw\sqrt{(Aw)^2 + 1} + 2Ax\sqrt{(2Ax)^2 + 1} + \operatorname{arsinh}(Aw) + \operatorname{arsinh}(2Ax)}{4A}$$

Substituting in the known arc length for the whole segment and simplifying it's found that:

$$L = \frac{Aw\sqrt{(Aw)^2 + 1} + \operatorname{arsinh}(Aw)}{2A}$$

It's difficult to solve this for A , so a numerical approach using Newton's method was taken to find the solution. The function $U(V)$ was defined:

$$U(V) = \frac{V\sqrt{(V)^2 + 1} + \operatorname{arsinh}(V)}{2V}$$

Note that

$$\frac{L}{w} = U(Aw)$$

$$U'(V) = \frac{V\sqrt{(V)^2 + 1} - \operatorname{arsinh}(V)}{2V^2}$$

This information was used to implement Newton's method, that would solve $U(V)$ using the known value $\frac{L}{w}$ and find the unknown value Aw that can be easily

solved for A . Once A is known, it's known from the definition of this parabolic segment that

$$0 = A \left(\pm \frac{w}{2} \right)^2 - B$$

Thus

$$B = \frac{Aw^2}{4}$$

The approximating curve of the bending rod is now known. To find the positions of the component bodies, it's known that at the equilibrium position of the rod, the component bodies are equidistant from each other due to having the same linear and torsional spring characteristics. Thus, for each node n_i with unknown starting position (x_i, y_i) , the arc length of the parabolic segment to that position is given by the known value:

$$S(x_i) = \frac{iL}{N-1}$$

Using the first fundamental theorem of calculus,

$$S'(x) = \sqrt{1 + 4A^2x^2}$$

Newton's method can now be employed to solve for the x positions of each component body, and the y positions can be found based on the definition of the parabolic segment

$$y = Ax^2 - B$$

An initial position for each component body can now be found in two dimensions, which can then be projected into three dimensions for the simulation. The computational cost for using Newton's method for solving the parabolic curve and each component position is minimal. Overall, it saves computational power by providing a good initial position for the rod's component bodies. This allows for convergent behavior upon initialization without requiring exceedingly small time steps.

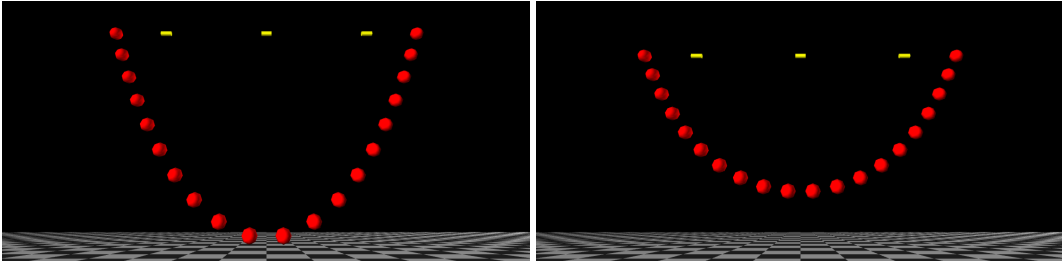


Figure A1: A red rod bent by a taut yellow cable. The left image shows the initial positions of the component bodies as determined by the parabolic approximation. The right image shows the bending rod after reaching equilibrium through the torsion and linear springs.

Appendix B

Aerodynamics Approximation

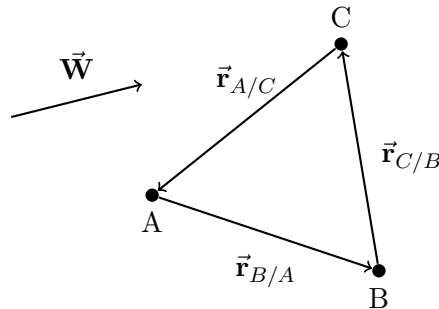
The aerodynamics of the tensegrity kite was heavily approximated. Aerodynamics was only simulated for the cloth of the kite, and ignored for the thin structural components. The cloth was split into four triangles, two large triangles at the front providing the main lift, and two small triangles at the back providing some stabilization. Aerodynamic calculations were performed on each triangle independently of one another, allowing each triangle to have the same implementation. The implementation of the aerodynamic calculations was inspired by the vortex lattice method but used aerodynamic equations specific for kites.

The application of the aerodynamics was split into three problems: calculating the forces of lift and drag, determining the center of pressure of the triangle, and then using the center of pressure to decompose the total force into equivalent forces on the triangle's anchor points. This implementation allowed creating aerodynamics that would apply to already existing simulated bodies, and would utilize the discrete implementation of the bending rods to create internal structural forces caused by the aerodynamic load.

B.0.1 Finding lift and drag

To find the forces of lift and drag, the problem was simplified using a set of assumptions. First, it was assumed that the relative air velocity \vec{w} was constant and did not significantly change relative to the triangle. Following from that assumption, it was also assumed that the problem could be projected into two dimensions where simple formulas for the aerodynamic forces could be applied, and then integrated back into three dimensions to find the total aerodynamic force.

Based on the implementation of the bending rod, it was known that the kite was going to be attached to three bodies, **A**, **B**, **C**, with positions A , B , C , velocities \vec{v}_A , \vec{v}_B , \vec{v}_C , and respective masses m_A , m_B , m_C . A constant wind velocity \vec{w} needed to be given, and the relative air velocity \vec{W} could be calculated using that velocity and the average velocity of the three particles. Relative rotational velocity was ignored for this part of the problem.



It was assumed that the drag force acts in the direction of the air velocity, and the lift force acts perpendicularly to the drag in the plane formed by the normal and the air velocity. Projecting this three dimensional problem into two dimensions would need to make use of those assumptions. It was also assumed that the wind was not normal to the triangle. From those assumptions, a new coordinate frame could be created that would be used for the purposes of projecting the problem into two dimensions.

First, we found the normal of the triangle \vec{n} :

$$\vec{n} = \vec{r}_{B/A} \times \vec{r}_{A/C}.$$

Note that we assumed that

$$\vec{n} \cdot \vec{W} \neq 0.$$

Now we can choose the normal to the triangle \vec{N} as the normal that is in a similar direction as the air velocity \vec{W} :

$$\vec{N} = \frac{\vec{n} \cdot \vec{W}}{|\vec{n} \cdot \vec{W}|} \vec{n}.$$

The two other vectors defining the coordinate frame will be \vec{B} which will be referred to as the binormal, and \vec{T} which will be referred to as the tangent. We can define them as the following:

$$\vec{B} = \vec{W} \times \vec{N}$$

$$\vec{T} = \vec{N} \times \vec{B}$$

The problem can now be rotated to a new coordinate frame formed by \hat{N} , \hat{B} , and \hat{T} where:

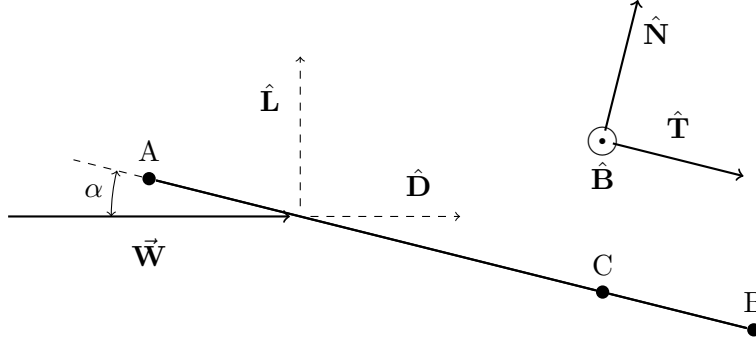
$$\hat{N} = \frac{\vec{N}}{|\vec{N}|}$$

$$\hat{B} = \frac{\vec{B}}{|\vec{B}|}$$

$$\hat{T} = \frac{\vec{T}}{|\vec{T}|}$$

It's also useful to define

$$\hat{W} = \frac{\vec{W}}{|\vec{W}|}$$



With this rotation, the problem can now be projected into two dimensions. The angle of attack is constant for each projection, and is given by

$$\alpha = \sin^{-1}(\hat{\mathbf{N}} \cdot \hat{\mathbf{W}}).$$

The directions of the drag force $\hat{\mathbf{D}}$ and lift force $\hat{\mathbf{L}}$ is the same for each projection and is given by:

$$\hat{\mathbf{D}} = \hat{\mathbf{W}}$$

$$\hat{\mathbf{L}} = \frac{\hat{\mathbf{N}} - (\hat{\mathbf{N}} \cdot \hat{\mathbf{D}}) \hat{\mathbf{D}}}{|\hat{\mathbf{N}} - (\hat{\mathbf{N}} \cdot \hat{\mathbf{D}}) \hat{\mathbf{D}}|}$$

Now, to find the magnitudes of the lift and drag force, we need to find the coefficient of lift c_l and the coefficient of drag c_d . To find these values, it's necessary to find the aspect ratio a of the kite. This is defined by:

$$a = \frac{s^2}{A_s}$$

where s is the wing span of the kite, defined by

$$s = \max(|\vec{\mathbf{r}}_{B/A} \cdot \hat{\mathbf{B}}|, |\vec{\mathbf{r}}_{C/B} \cdot \hat{\mathbf{B}}|, |\vec{\mathbf{r}}_{A/C} \cdot \hat{\mathbf{B}}|)$$

and A_s is the surface area of the kite, defined by

$$A_s = \frac{1}{2} |\vec{\mathbf{r}}_{B/A} \times \vec{\mathbf{r}}_{A/C}|$$

It's assumed that the coefficients of lift and drag for the triangle kite can be found by the following equations that use the now defined aspect ratio a :

$$c_{l0} = 2\pi\alpha$$

$$c_{d0} = 1.28 \sin(\alpha)$$

$$c_l = \frac{c_{l0}}{1 + \frac{c_{l0}}{\pi a}}$$

$$c_d = c_{do} + \frac{c_l^2}{0.7\pi a}$$

The magnitude of the lift force $|\vec{\mathbf{L}}|$ and the drag force $|\vec{\mathbf{D}}|$ can be found by the lift and drag formulas:

$$|\vec{\mathbf{L}}| = \frac{1}{2}c_l A_s \rho |\vec{\mathbf{W}}|^2$$

$$|\vec{\mathbf{D}}| = \frac{1}{2}c_d A_s \rho |\vec{\mathbf{W}}|^2$$

Finally, the lift and drag force vectors can now be found.

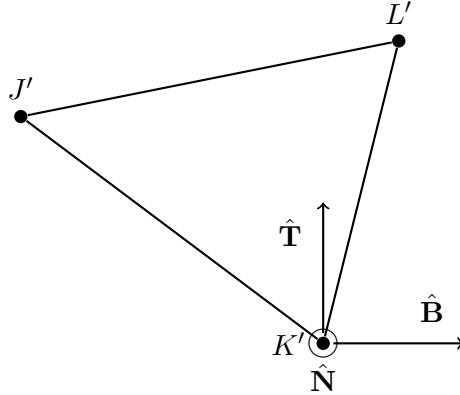
$$\vec{\mathbf{L}} = |\vec{\mathbf{L}}|\hat{\mathbf{L}}$$

$$\vec{\mathbf{D}} = |\vec{\mathbf{D}}|\hat{\mathbf{D}}$$

B.0.2 Finding center of pressure

Creating the coordinate frame

To make finding the center of pressure easier, we will define a new coordinate frame formed by the previously calculated orthonormal vectors $\hat{\mathbf{B}}$, $\hat{\mathbf{T}}$, and $\hat{\mathbf{N}}$.



The translation and rotation of a point Q in the original coordinate frame to the point Q' in the new coordinate frame can be calculated through the following operation:

$$R = \begin{bmatrix} \hat{\mathbf{B}}_x & \hat{\mathbf{B}}_y & \hat{\mathbf{B}}_z \\ \hat{\mathbf{T}}_x & \hat{\mathbf{T}}_y & \hat{\mathbf{T}}_z \\ \hat{\mathbf{N}}_x & \hat{\mathbf{N}}_y & \hat{\mathbf{N}}_z \end{bmatrix}$$

$$Q' = R\vec{\mathbf{r}}_{Q/K}$$

where $\vec{\mathbf{K}}$ is the vector representing the point in the old coordinate frame that becomes the origin of the new coordinate frame. The vector representing the point P in the original frame can be calculated from its respective vector representing the point P' in the new frame by the following operation:

$$\vec{\mathbf{P}} = R^T \vec{\mathbf{P}}' + \vec{\mathbf{K}}$$

Now, we can rename the vertices of the triangle ABC to the equivalent triangle JKL , where the vertex K will lie at the origin of the new coordinate frame. We can then translate and rotate the triangle JKL to $J'K'L'$ by:

$$J' = R\vec{\mathbf{r}}_{J/K}$$

$$K' = R\vec{\mathbf{r}}_{K/K}$$

$$L' = R\vec{\mathbf{r}}_{L/K}$$

Thus, subject to the order in which the vertices are renamed:

$$J' = \begin{pmatrix} J'_B \\ J'_T \\ 0 \end{pmatrix} \quad K' = \begin{pmatrix} 0 \\ 0 \\ 0 \end{pmatrix} \quad L' = \begin{pmatrix} L'_B \\ L'_T \\ 0 \end{pmatrix}$$

$$J'_B \leq 0 < L'_B$$

Note that the third N -coordinates are all zero because K' is placed at the origin, and by definition of the normal,

$$\vec{\mathbf{r}}_{J/K} \cdot \hat{\mathbf{N}} = 0$$

$$\vec{\mathbf{r}}_{L/K} \cdot \hat{\mathbf{N}} = 0$$

Assumptions

We know that the total force $\vec{\mathbf{F}}$ on triangle ABC is given by:

$$\vec{\mathbf{F}} = \vec{\mathbf{L}} + \vec{\mathbf{D}}$$

We can define $\vec{\mathbf{F}}'$ as:

$$\vec{\mathbf{F}}' = R\vec{\mathbf{F}}$$

We assume that this total force can be found by summing a distributed force about the whole triangle. In other words, if $\vec{\mathbf{F}}'(b, t)$ is the force generated at point $(b, t, 0)$ on the triangle $J'K'L'$, then

$$\iint_A \vec{\mathbf{F}}'(b, t) dA = \vec{\mathbf{F}}' \quad (\text{A1})$$

We also assume that the distributed force always acts in the same direction. In other words:

$$\hat{\mathbf{F}}' = \frac{\vec{\mathbf{F}}'}{|\vec{\mathbf{F}}'|} = \frac{\vec{\mathbf{F}}'(b, t)}{|\vec{\mathbf{F}}'(b, t)|} \quad (\text{A2})$$

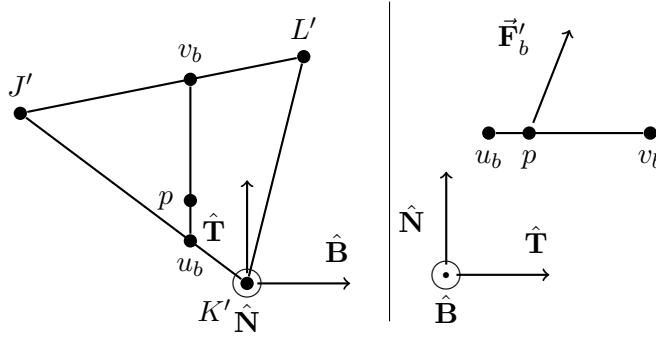
We assumed earlier that the force of drag acts in the direction of the air velocity, and that the force of lift acts perpendicular to the force of drag in the plane formed by the triangle normal and the wind. Thus the rotated force vector $\hat{\mathbf{F}}'$ can be decomposed into its coordinates:

$$\hat{\mathbf{F}}' = \begin{bmatrix} 0 \\ f_T \\ f_N \end{bmatrix} \quad (\text{A3})$$

Note that the B -coordinate is zero because no force acts in the $\hat{\mathbf{B}}$ direction.

Next, we make two assumptions about the lift and drag for a cross section of the triangle $J'K'L'$ in the $\hat{\mathbf{B}}$ direction, with boundary points

$$u = \begin{pmatrix} b \\ u_b \\ 0 \end{pmatrix}, v = \begin{pmatrix} b \\ v_b \\ 0 \end{pmatrix}$$



First, we assume that the magnitude of the force $\vec{\mathbf{F}}'_b$ generated by that cross-section is proportional to the length of the cross section. Thus, for some constant c :

$$|\vec{\mathbf{F}}'_b| = c(v_b - u_b)$$

If we combine this with assumption A2, we find that,

$$\vec{\mathbf{F}}'_b = c(v_b - u_b)\hat{\mathbf{F}} \quad (\text{A4})$$

Second, we assume that the center of pressure p of this cross section has a T -coordinate that is a k -ratio away from the leading edge. In practice, k will be equal to $\frac{1}{4}$, so that the center of pressure for the cross section will be $\frac{1}{4}$ the length from the leading edge. Therefore:

$$p = \begin{pmatrix} b \\ p_b \\ 0 \end{pmatrix} \quad (\text{A5})$$

$$p_b = k(v_b - u_b) + u_b$$

Calculating the center of pressure

We'll define the center of pressure P for the triangle as

$$P = \begin{pmatrix} P_x \\ P_y \\ P_z \end{pmatrix}$$

This point is what we'll be solving for. We can define P' as the equivalent point in the rotated coordinate frame, with:

$$P' = R\vec{r}_{P/K} = \begin{pmatrix} P'_B \\ P'_T \\ P'_N \end{pmatrix}$$

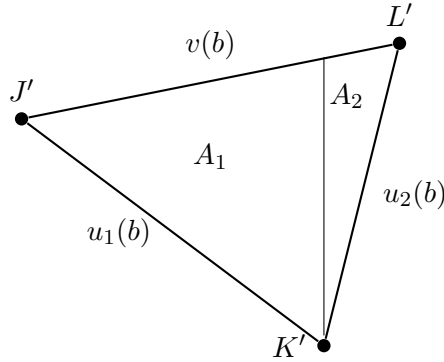
We know that the moment about the center of pressure caused by the aerodynamic forces is zero, so using assumption A1 for the triangle $J'K'L'$:

$$\iint_A (\vec{r} - \vec{P}') \times \vec{F}'(b, t) dA = 0$$

where

$$\vec{r} = \begin{bmatrix} b \\ t \\ 0 \end{bmatrix}$$

Based on the construction of triangle $J'K'L'$, there is a discontinuity at the origin. Therefore the integral needs to be split into two separate areas:



$$\iint_{A_1} (\vec{r} - \vec{P}') \times \vec{F}'(b, t) dA + \iint_{A_2} (\vec{r} - \vec{P}') \times \vec{F}'(b, t) dA = 0$$

If we define $u_1(b)$ as the line from J' to K' , $u_2(b)$ as the line from K' to L' , and $v(b)$ as the line from J' to L' , then the limits of integration can be found:

$$u_1(b) = \frac{J'_T}{J'_B} b$$

$$u_2(b) = \frac{L'_T}{L'_B}b$$

$$v(b) = \frac{L'_T - J'_T}{L'_B - J'_B}(b - L'_B) + L'_T$$

$$\int_{J'_B}^0 \int_{u_1(b)}^{v(b)} (\vec{\mathbf{r}} - \vec{\mathbf{P}}') \times \vec{\mathbf{F}}'(b, t) dt db + \int_0^{K'_B} \int_{u_2(b)}^{v(b)} (\vec{\mathbf{r}} - \vec{\mathbf{P}}') \times \vec{\mathbf{F}}'(b, t) dt db = 0$$

We can decompose $\vec{\mathbf{F}}'(b, t)$ to its magnitude and direction

$$\vec{\mathbf{F}}'(b, t) = |\vec{\mathbf{F}}'(b, t)| \hat{\mathbf{F}}'(b, t)$$

and use assumption A2 and A3 to get:

$$\vec{\mathbf{F}}'(b, t) = |\vec{\mathbf{F}}'(b, t)| \begin{bmatrix} 0 \\ f_T \\ f_N \end{bmatrix}$$

Using that to simplify the cross product the integral becomes:

$$\int_{J'_B}^0 \int_{u_1(b)}^{v(b)} |\vec{\mathbf{F}}'(b, t)| \begin{bmatrix} (t - P_T)f_N - f_T P_N \\ -(b - P_B)f_N \\ (b - P_B)f_N \end{bmatrix} dt db + \int_0^{K'_B} \int_{u_2(b)}^{v(b)} |\vec{\mathbf{F}}'(b, t)| \begin{bmatrix} (t - P_T)f_N - f_T P_N \\ -(b - P_B)f_N \\ (b - P_B)f_N \end{bmatrix} dt db$$

It can be shown that to evaluate the integral with respect to t , only two key integrals need to be found:

$$\int_{u(b)}^{v(b)} |\vec{\mathbf{F}}'(b, t)| dt$$

$$\int_{u(b)}^{v(b)} t |\vec{\mathbf{F}}'(b, t)| dt$$

From assumption A4 it follows that

$$\int_{u(b)}^{v(b)} |\vec{\mathbf{F}}'(b, t)| dt = c(v(b) - u(b))$$

Using assumption A5 as the center of pressure for a segment with respect to t , and undergoing a similar integral process it can be shown that:

$$\int_{u(b)}^{v(b)} t |\vec{\mathbf{F}}'(b, t)| dt = c(v(b) - u(b))p(b)$$

where $p(b)$ is the p_b from assumption A5 evaluated at the bounds $u(b)$ and $v(b)$.

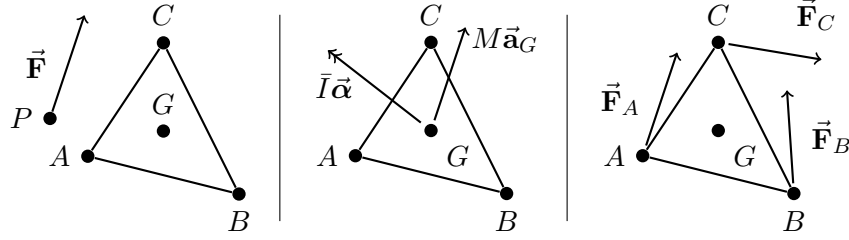
Enough information is now known to evaluate the integral and solve for the center of pressure. A symbolic math computer package was used to find and simplify the solution. Many of the introduced terms cancel out in the operation, and the center of pressure in the new coordinate frame P' is found to be:

$$P' = \begin{pmatrix} \frac{J_B + L_B}{J_B J_T - L_B L_T + \frac{3}{2} J_B L_T k - 2 L_B J_T k} \\ \frac{3(J_B - L_B)}{0} \end{pmatrix}$$

This can be converted back to P in the original coordinate frame using R^T .

B.0.3 Force Decomposition

We now know the resultant force and location of the aerodynamic load on the triangle. However, the triangle is created by three anchor bodies, and thus the force at the center of pressure needs to be decomposed to an equivalent three forces at the anchor bodies. This is done by treating the three anchor bodies as a singular rigid body, finding the linear and angular acceleration of the rigid body caused by the aerodynamic forces, then finding the linear acceleration of each anchor body that composes the rigid body, and converting that linear acceleration into an equivalent force to be applied to the anchor body. This approach works because the internal forces between the anchor bodies are already simulated by the tensegrity structure, allowing the anchor bodies to be treated as a virtual rigid body at each time step.



The first step is to treat the anchor bodies as components of a rigid body. This rigid body has a total mass of M with

$$M = m_A + m_B + m_C$$

The position of the center of pressure is the mass weighted average of the center of mass of the three bodies

$$\vec{G} = \frac{m_A \vec{A} + m_B \vec{B} + m_C \vec{C}}{M}$$

We can then define \vec{a} , \vec{b} , \vec{c} as the positions of bodies A , B , C , relative to the center of mass, and \vec{p} as the position of the applied force relative to the center of mass.

$$\vec{a} = \vec{A} - \vec{G}$$

$$\vec{b} = \vec{B} - \vec{G}$$

$$\vec{c} = \vec{C} - \vec{G}$$

$$\vec{p} = \vec{P} - \vec{G}$$

We can now find the moment of inertia about the center of mass \bar{I}

$$\bar{I}_{xx} = m_A(a_y^2 + a_z^2) + m_B(b_y^2 + b_z^2) + m_c(c_y^2 + c_z^2)$$

$$\bar{I}_{yy} = m_A(a_x^2 + a_z^2) + m_B(b_x^2 + b_z^2) + m_c(c_x^2 + c_z^2)$$

$$\bar{I}_{zz} = m_A(a_x^2 + a_y^2) + m_B(b_x^2 + b_y^2) + m_c(c_x^2 + c_y^2)$$

$$\begin{aligned}
\bar{I}_{xy} &= m_A a_x a_y + m_B b_x b_y + m_C c_x c_y \\
\bar{I}_{yz} &= m_A a_y a_z + m_B b_y b_z + m_C c_y c_z \\
\bar{I}_{xz} &= m_A a_x a_z + m_B b_x b_z + m_C c_x c_z \\
\bar{I} &= \begin{bmatrix} \bar{I}_{xx} & -\bar{I}_{xy} & -\bar{I}_{xz} \\ -\bar{I}_{xy} & \bar{I}_{yy} & -\bar{I}_{yz} \\ -\bar{I}_{xz} & -\bar{I}_{yz} & \bar{I}_{zz} \end{bmatrix}
\end{aligned}$$

Now we know enough to solve the linear acceleration of the triangle body $\vec{\mathbf{a}}_G$.

$$\vec{\mathbf{a}}_G = \frac{\vec{\mathbf{F}}}{M}$$

The angular acceleration $\vec{\boldsymbol{\alpha}}$ can be solved by solving the matrix equation

$$\bar{I}\vec{\boldsymbol{\alpha}} = \vec{\mathbf{p}} \times \vec{\mathbf{F}} - \vec{\boldsymbol{\omega}} \times \bar{I}\vec{\boldsymbol{\omega}}$$

where $\vec{\boldsymbol{\omega}}$ is the rotational velocity of the triangle. With those known, the expected acceleration of each body caused by the aerodynamic load can be calculated

$$\begin{aligned}
\vec{\mathbf{a}}_A &= \vec{\mathbf{a}}_G + \vec{\boldsymbol{\alpha}} \times \vec{\mathbf{a}} \\
\vec{\mathbf{a}}_B &= \vec{\mathbf{a}}_G + \vec{\boldsymbol{\alpha}} \times \vec{\mathbf{b}} \\
\vec{\mathbf{a}}_C &= \vec{\mathbf{a}}_G + \vec{\boldsymbol{\alpha}} \times \vec{\mathbf{c}}
\end{aligned}$$

Those expected accelerations can then be converted into applied forces:

$$\begin{aligned}
\vec{\mathbf{F}}_A &= m_A \vec{\mathbf{a}}_A \\
\vec{\mathbf{F}}_B &= m_B \vec{\mathbf{a}}_B \\
\vec{\mathbf{F}}_C &= m_C \vec{\mathbf{a}}_C
\end{aligned}$$

Through this method, the calculated aerodynamic force can now be applied at the center of pressure, and decomposed to equivalent forces at the three anchor bodies of the sail for the physics simulation.

B.0.4 Limitations

This is a heavily approximated method of generating aerodynamic forces. The analysis ignores turbulence, ignores the local effects on the wind that the sails would create, and ignores many other aerodynamic factors. A lot of the formulas used depended on small angle approximations, which we ignored. We did attempt to mitigate the effect of a lack of turbulence in our analysis by introducing random noise to the wind vector in each step of the physics simulation. We did not have a strong background in aerodynamics, so we do not know how to quantify the error of our methods. Thus, we could only measure the success of the aerodynamics through visual inspection.

Appendix C

References

1. Jiaming Zha, Xiangyu Wu, Joseph Kroeger, Natalia Perez, and Mark W. Mueller. A collision-resilient aerial vehicle with icosahedron tensegrity structure. In *IROS 2020*, March 2020.
2. Vytas SunSpiral, Adrian Agogino, and David Atkinson. Super ball bot - structures for planetary landing and exploration, 2015.
3. Steven Lessard, Pattawong Pansodtee, Ash Robbins, Leya Breanna Baltaxe-Admony, James M Trombadore, Mircea Teodorescu, Adrian Agogino, and Sri Kurniawan. Crux: a compliant robotic upper-extremity exosuit for lightweight, portable, multi-dof muscular augmentation, 2017.
4. Atil Iscen, Adrian Agogino, Vytas SunSpiral, and Kagan Tumer. Robust distributed control of rolling tensegrity robot. In *The Autonomous Robots and Multirobot Systems (ARMS) workshop at AAMAS 2013*, 2013.
5. Andrew P Sabelhaus, Jonathan Bruce, Ken Caluwaerts, Yangxin Chen, Dizhou Lu, Yuejia Liu, Adrian K Agogino, Vytas SunSpiral, and Alice M Agogino. Hardware Design and Testing of SUPERball, a Modular Tensegrity Robot. In *Proceedings of the 6th World Conference of the International Association for Structural Control and Monitoring (6WCSCM)*, 2014.
6. Bjorn Johnson and Adrian Agogino. Feasibility analysis of unmanned aerial vehicle based on tensegrity structure, 2021.
7. cannon-es. <https://github.com/pmndrs/cannon-es>. 2016.
8. Ricardo Cabello. <https://threejs.org/>. 2010.

REPORT DOCUMENTATION PAGE				Form Approved OMB No. 0704-0188	
<p>The public reporting burden for this collection of information is estimated to average 1 hour per response, including the time for reviewing instructions, searching existing data sources, gathering and maintaining the data needed, and completing and reviewing the collection of information. Send comments regarding this burden estimate or any other aspect of this collection of information, including suggestions for reducing this burden, to Department of Defense, Washington Headquarters Services, Directorate for Information Operations and Reports (0704-0188), 1215 Jefferson Davis Highway, Suite 1204, Arlington, VA 22202-4302. Respondents should be aware that notwithstanding any other provision of law, no person shall be subject to any penalty for failing to comply with a collection of information if it does not display a currently valid OMB control number.</p> <p>PLEASE DO NOT RETURN YOUR FORM TO THE ABOVE ADDRESS.</p>					
1. REPORT DATE (DD-MM-YYYY) 01-06-2022		2. REPORT TYPE Technical Memorandum		3. DATES COVERED (From - To)	
4. TITLE AND SUBTITLE Design, Control, and Simulation of Tensegrity Based Kites				5a. CONTRACT NUMBER	
				5b. GRANT NUMBER	
				5c. PROGRAM ELEMENT NUMBER	
6. AUTHOR(S) Nathan Scheinkman, Bjorn Johnson, Abed Musaffar, Adrian Agogino				5d. PROJECT NUMBER	
				5e. TASK NUMBER	
				5f. WORK UNIT NUMBER	
7. PERFORMING ORGANIZATION NAME(S) AND ADDRESS(ES) NASA Ames Research Center Moffett Field, California 94035				8. PERFORMING ORGANIZATION REPORT NUMBER L-	
9. SPONSORING/MONITORING AGENCY NAME(S) AND ADDRESS(ES) National Aeronautics and Space Administration Washington, DC 20546-0001				10. SPONSOR/MONITOR'S ACRONYM(S) NASA	
				11. SPONSOR/MONITOR'S REPORT NUMBER(S) NASA/TM-202220220009943	
12. DISTRIBUTION/AVAILABILITY STATEMENT Unclassified-Unlimited Subject Category 63 Availability: NASA STI Program (757) 864-9658					
13. SUPPLEMENTARY NOTES An electronic version can be found at http://ntrs.nasa.gov .					
14. ABSTRACT Due to lowering price and increased functionality, the future could bring in a huge number of UAVs flying in urban areas. In order to safely accommodate them, they should be fundamentally safe to fly. Unfortunately, current rigid designs could cause significant damage in case of a crash. To mitigate this problem, this report proposes constructing soft UAVs using tensegrity structures in order to mitigate the impact of collisions, effectively improving the safety of the vehicles and increasing public confidence in the use of UAVs. In this paradigm, the frame of the vehicle is designed using a tensegrity structure, a geometric structure composed of suspended elements of pure compression and pure tension, which during a collision can better absorb high stresses through elastic deformation. As a feasibility study we test this concept on an actuated tensegrity kite in a custom physics simulator, designed to simulate tensegrity structures with non-rigid rods, along with basic simulations of lift. Results show that this concept is feasible and that the kite can change orientation by actively changing the shape of the tensegrity structure.					
15. SUBJECT TERMS aerodynamics, tensegrity, flexible, UAS					
16. SECURITY CLASSIFICATION OF:			17. LIMITATION OF ABSTRACT	18. NUMBER OF PAGES	19a. NAME OF RESPONSIBLE PERSON
a. REPORT	b. ABSTRACT	c. THIS PAGE			STI Information Desk (help@sti.nasa.gov)
U	U	U	UU		19b. TELEPHONE NUMBER (Include area code) (757) 864-9658

